On the proton radiography of magnetic fields in targets irradiated by intense picosecond laser pulses

N D Bukharskii[1], Y V Kochetkov[1], M Ehret[2,3], K L Gubskiy[1], A P Kuznetsov[1], J J Santos[2], B Zielbauer[4], Y Abe[5], F Law[5], Ph A Korneev[1,6]

[1] National Research Nuclear University MEPhI, Moscow, Russian Federation
[2] Laboratoire CELIA, Université de Bordeaux, France
[3] Institut für Kernphysik, Technische Universität Darmstadt, Germany
[4] PP/PHELIX, GSI, Darmstadt, Germany
[5] Institute of Laser Engineering, Osaka University, Japan
[6] Lebedev Physical Institute, Moscow, Russian Federation

E-mail: n.bukharskii@gmail.com

Abstract. Proton radiography is a common diagnostic technique in laser-driven magnetic field generation studies. It is based on measuring proton beam deflection in electromagnetic fields induced around the target with the help of radiochromic film stacks. Unraveling information recorded in experimental radiographs and extracting the field profiles is not always a straightforward task. In this paper, some aspects of data analysis by reproducing experimental radiographs in numerical simulations are described. The approach allows determining the field strength and structure in the target area for various target geometries.

1. Introduction

Strong magnetic field generators potentially have a number of applications in different areas of science and technology. One of them is controlling high-energy charged particles transport, e.g. collimation of divergent fast electron beams in fast ignition approach to inertial confinement fusion. Another possible application concerns the area of laboratory astrophysics where strong magnetic fields can be used to create magnetized plasma and model various astrophysical phenomena. A prospective way of magnetic field generation is laser-driven magnetic field generation [1]. This method is compact, does not require capacitor banks and allows producing magnetic fields well in excess of 100 T, which is beyond the limit for conventional methods relying on non-destructive resistive and superconductive electromagnets.

Laser-driven magnetic field generation implies irradiating targets with intense short laser pulses. Focusing of such pulses into a small spot on the target surface leads to the creation of hot electrons, which leave the target surface and generate strong discharge currents. For certain target geometries this return flow can have a dedicated direction and thus produce high magnetic fields in the interaction region. Depending on the duration of the pulse, the field may be more or less stationary, however it is also limited by target impedance, including all kinds of losses. To come closely to the stationary regime, the laser pulse duration should be longer than the time necessary to connect the current circuit in the target. In nanosecond regime this means the circuit perimeter should be less than hundreds of mm, while in picosecond regime the target size should be three orders less, about few hundreds of microns.

2. Proton radiography setup

In order to study generated magnetic fields qualitatively and quantitatively various techniques can be employed – B-dot probes, optical diagnostics, spectrometry and proton radiography [2]. The latter allows measuring magnetic and electric fields in the target region and tracking their evolution on a

picosecond time scale [3]. Principal scheme of the setup for proton radiography with two laser beams is shown in Figure 1.

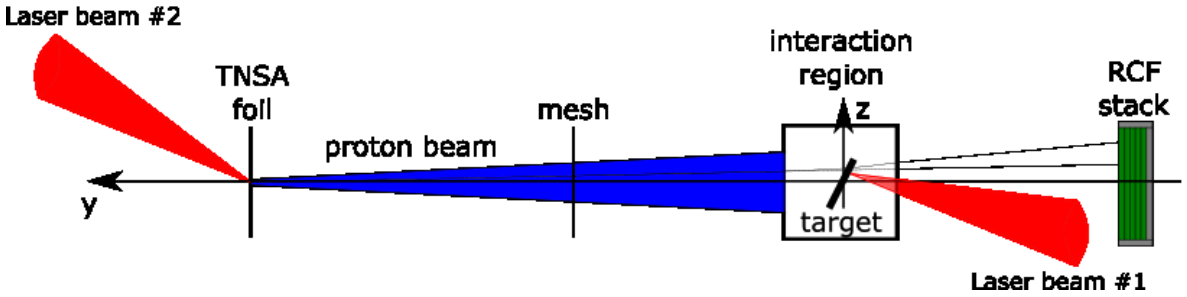

Figure 1. Principal scheme of proton radiography.

Proton beam is created via TNSA mechanism [4] under irradiation of a thin metallic foil by an auxiliary intense laser pulse. The proton beam is directed to come through the region of interest, where the main laser pulse interacts with the studied target. In this region, protons under the action of the Lorentz force deflect from their initial trajectories and form some structure on radio-chromic films (RCF). The active layer of RCF contains a marker dye changing its color when exposed to ionizing radiation, thus allowing RCF to be used for measuring the spatial distribution of proton density in the probe beam. As the target itself also serves as a proton source, a metallic mesh may be placed in the way of the TNSA proton beam. It forms a periodic structure in the probe beam, which can be used to distinguish diagnostic protons from the target protons in the radiograph. Since stopping range of ions in matter varies with their energy, different layers of RCF stack register protons of different energies passing the interaction region at different moments of time, which enables performing time-resolved measurements [5].

The main parameters of TNSA probe beam are its divergence, proton energy distribution and proton density. For TNSA mechanism, the divergence of the probe beam is of the order of several degrees. Low energy part of the signal (< 1 MeV) containing the contribution from heavy ions present in the TNSA beam may be cut by placing a thin ($\sim 10\ \mu m$) metallic foil before the very first layer of the stack to avoid saturation. Therefore, energies of detected protons lie in the range from 1 MeV to the maximum proton energies, depending on the properties of the used laser beam. It allows tracking the time evolution of electromagnetic fields on the scale of several hundred picoseconds with the resolution of less than 10 ps. Proton densities in the beam can be estimated by first calculating the layer exposure to dose of ionizing radiation using the "RGB channel gray value – dose in gray" calibration data for a particular type of radio-chromic film. Then this dose can be used to determine the total energy depleted in the active layer and with it calculate the number of protons in the beam and their density. It allows estimation of different effects in the probe proton beam, as e.g. collective charge-separation or diamagnetic effects [6].

For time-resolved measurements one needs to know the distribution of protons of different energies between different RCF layers. This information can be acquired using computer programs for calculation of transport of ions in matter such as SRIM/TRIM [7]. An illustration depicting where which protons are absorbed for a typical RCF-stack setup consisting of 12 μm aluminium foil filter, 5 HD-V2 films and 4 more sensitive EBT-3 films placed further in the stack is given in Figure 2.

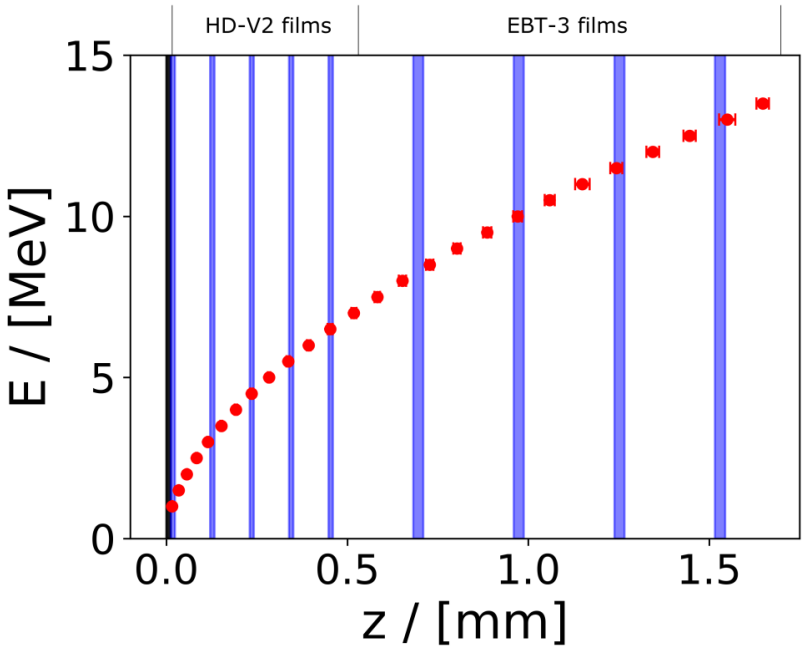

Figure 2. An illustration of proton energy distribution in RCF-stack layers for a stack consisting of 12 μm aluminium foil filter (marked with black), 5 HD-V2 films and 4 EBT-3 films (the active layers marked with blue).

As one can see, the energy of protons absorbed in the active layer of the first film is about 1..3 MeV, in the active layer of the second film – about 3..4 MeV, the third film – 4..5 MeV and so on. The time of flight difference and therefore time resolution for a distance of 3 mm between the TNSA foil and the studied target is 20 ps for the 2nd and 3rd layer pair and less for the subsequent pairs. The overall range of time resolved measurements is about 160 ps, providing all the layers are activated.

3. Numerical simulations of radiographic images

A standard way to extract information about the fields from the experimental radiographs is performing numerical simulations of the proton flight through the target region. Roughly, comparing the simulated radiograph with the real one enables one to scale the fields that were used in the simulation and iteratively correct their structure to minimize the difference between the radiographs. When this difference becomes small enough, it is assumed that the fields in the interaction region are reconstructed with admissible error. Time-dependence of the fields are not considered for individual proton path, which is reasonable for a stationary regime of the magnetic field generation. For the faster processes, the error increases also because of the intrinsic time averaging. More universal modelling with e.g. Particle-In-Cell codes is possible, but it requires much more CPU time. Here only quasi-stationary situations are considered.

The simulation algorithm presented in this work can be divided into several steps. First, magnetic and electric fields formed near the target are determined assuming a unitary current and charge value. For calculation of the former a current contour is selected. Then it is divided into N small linear segments and Bio-Savart law is applied to find the total magnetic field $\boldsymbol{B}(\boldsymbol{r})$ from all segments at position $\boldsymbol{r}$:

$$\boldsymbol{B}(\boldsymbol{r}) = \frac{\mu_0}{4\pi}\sum_{i=1}^{N}\frac{I_i d\boldsymbol{l_i} \times \boldsymbol{r_i'}}{\left|\boldsymbol{r_i'}\right|^3} \quad (1)$$

where i is the number of a segment, I_i is the current in each segment, $d\boldsymbol{l_i}$ is a vector with direction matching that of the current and magnitude matching the length of the segment, $\boldsymbol{r_i'}$ is the displacement vector from the segment to the point at which the field is calculated. Electric field $\boldsymbol{E}(\boldsymbol{r})$ can be calculated assuming the target is charged to a certain potential. When the electromagnetic fields are defined, ballistic simulations are performed. For this purpose, differential equations describing the motion of a charged particle in the presence of the Lorentz force are solved for each proton in the beam separately:

$$m_p \frac{d^2 \boldsymbol{r_i}}{dt^2} = q_p \left(\boldsymbol{E}(\boldsymbol{r_i}) + \frac{d\boldsymbol{r_i}}{dt} \times \boldsymbol{B}(\boldsymbol{r}) \right), \quad (2)$$

where i is the number of a proton in the beam, $\boldsymbol{r_i}$ is its current position, m_p and q_p are the mass and charge of proton respectively. For the considered energies, nonrelativistic equation is used. Points in the RCF film plane with coordinates matching those of some probe proton are marked with '1', otherwise – with '0'. The resulted 2D array is saved as an image.

4. Characteristic features of the radiographs

The characteristic structures of radiographs can be demonstrated in simulations for a solenoidal-like current, i.e. assuming the target is a ring with uniform current circulating along its surface. It is shown in Figure 3 for different probing geometries. For all the simulations presented in this paper a shadow of the mesh, placed in the way of probe protons, was accounted for.

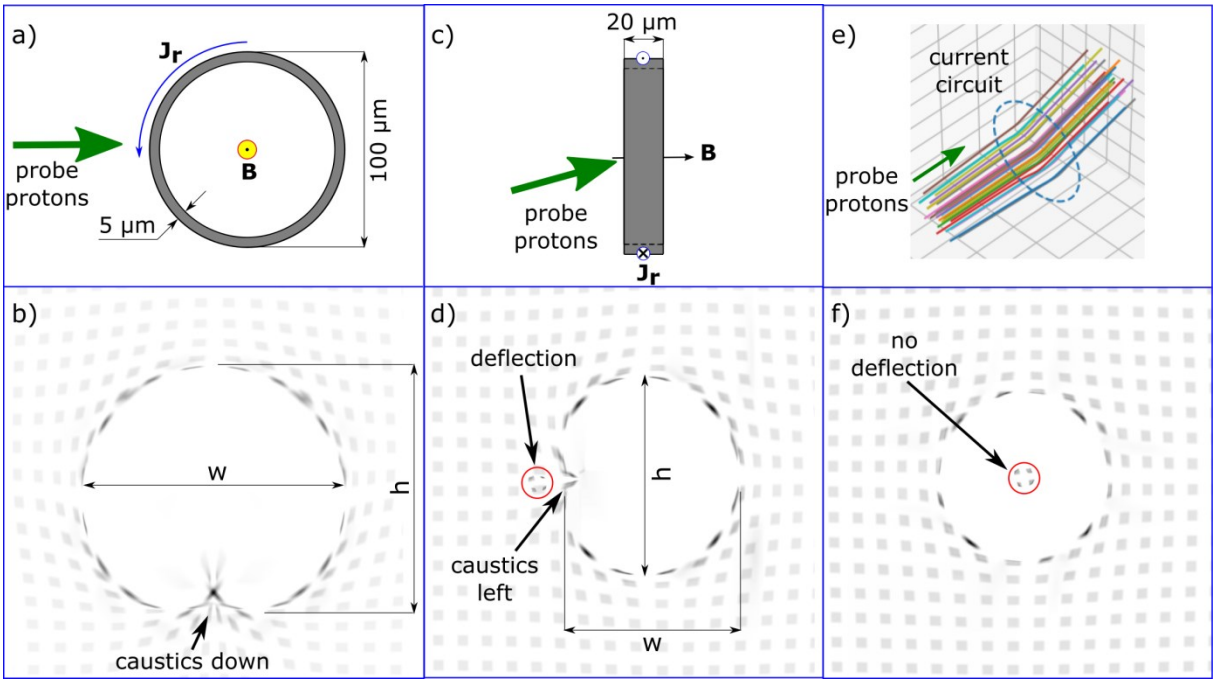

Figure 3. Proton radiographs on the example of the ring current circuit. a), c) – illustration of two probing geometries – perpendicular to the target axis and almost parallel to it respectively; b), d) – corresponding simulated radiographs; e) illustration of deflection for protons passing through the target centre; f) simulated radiograph for quasi-parallel probing geometry.

The structure (Figure 3b and Figure 3d) can be described as a "blob" with a reflection symmetry, inside which no proton signal is observed. The boundary of this "blob" is a thin and bright line where proton concentration is the highest. On one side of the image the boundary line intersects itself forming a distinct "caustic like" feature. The position of this feature depends on the relative orientation of the probe beam and the target magnetic field, thus allowing it to be used to determine the direction of the latter in experiment. For probing geometry a), i.e. in the plane perpendicular to the direction of the magnetic field, the caustics are either down or up depending on the direction of the return current flow. For probing geometry c), i.e. in the plane parallel to the magnetic field at a small angle to the target axis, the caustics are situated either on the left or on right side of the radiograph. A group of protons deflected to the left from the "blob" centre can also be seen on the radiograph corresponding to the almost parallel probing geometry. This group is formed by the protons that pass through the centre of the target, which is illustrated in Figure 3e. If the probing is done strictly parallel to the

direction of the formed magnetic field, the radiograph (Figure 3f) is symmetric, has no "caustic like" features and no deflection is observed for the protons passing the centre of the target.

Such bright line and "caustic like" features are commonly observed in the experimental radiographs. According to the theory of their formation given in [8] they appear due to the nonlinear nature of proton imaging when a finite area surface element in the object plane is mapped to a zero area element in the image plane. In theory it should lead to an infinite increase of proton intensity for this particular surface element in the image plane, but due to finite resolution of radio-chromic films the observed increase is several times the background proton intensity. As stated in [8], the condition for the appearance of nonlinear features is $\frac{l\alpha}{a} \gtrsim 1$, where l is the distance from the quasi-point proton source to the target, a is the characteristic scale of the electromagnetic perturbation and α is the deflection angle. So both magnetic and electric fields can be responsible for the caustics formation if they are high enough to cause significant deflection ($\alpha \gtrsim \frac{a}{l}$), yet the structure they form is different. Direct comparison of the magnetic field and electric field imprint for ring current circuit probed perpendicular to the ring axis is given in Figure 4.

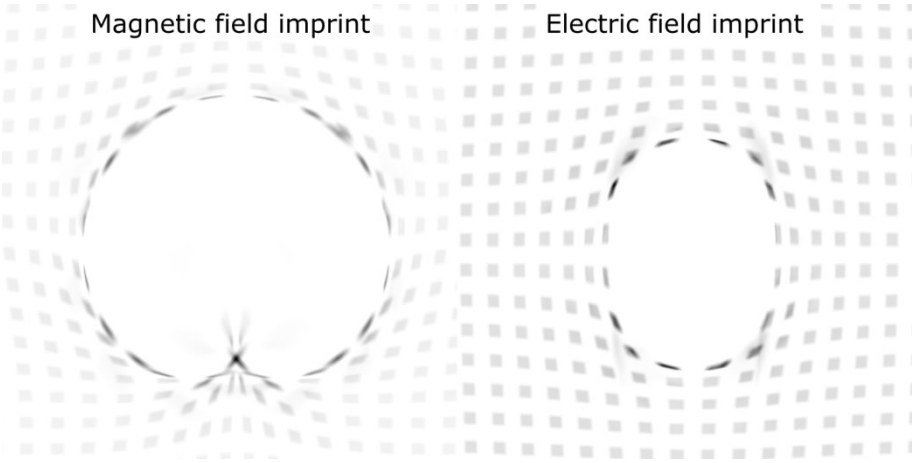

Figure 4. Comparison of the magnetic field and electric field imprint for ring current circuit probed perpendicularly to the ring axis.

5. Analyzing the radiographs

Different ways of analyzing experimental radiographs via numerical simulations are possible. In a relatively simple situation, as described above, they may rely on measuring the geometric parameters of the "blob" structure – namely its width w and height h. Their values change with the magnitude of the magnetic and electric field allowing the latter two to be estimated by matching the geometrical parameters of the simulated radiograph with those of the experimental one. Maps showing dependence of the width and height of the simulated "blob" on the magnetic field at the centre of the target and the electric potential of the target for the ring probed in a) geometry are shown in Figure 5.

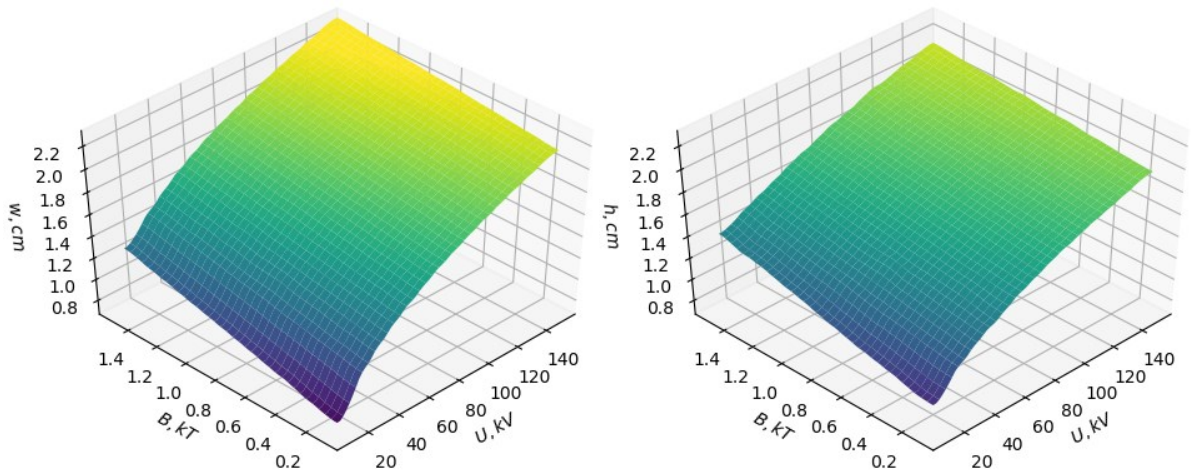

Figure 5. Maps showing dependence of geometric parameters of the simulated radiograph image structure (left – width of the "blob", right – height of the "blob") on the magnetic field at the target centre and on the electric potential of the target.

Measuring the values of w and h of the structure in the experimental radiograph allows one to draw $w = w_{exp}$ and $h = h_{exp}$ planes intersecting $w(U,B)$ and $h(U,B)$ surfaces. The intersection of each plane with the corresponding surface is a 2D curve which can be interpreted as a set of all possible U and B pairs for which the width or height of the simulated "blob" matches those values of the experimental "blob". The point where two resultant curves cross one another is the point where values of U and B are most likely the closest to the experimental ones. Since $w(U,B)$ and $h(U,B)$ functions have similar behavior it may be impossible to find the intersection of the fit to experimental values 2D curves with admissible error due to the small crossing angle between them. In order to avoid it other geometrical parameters of the radiograph structure may be introduced. If their dependence on the values of U and B is different from that of w and h, the crossing angle for this geometrical parameter will be higher and thus it will be possible to find the optimal values of U and B with less error.

Other possible ways of analyzing radiographs are correlation analysis and machine learning. By comparing the real radiograph with results of the simulation for a set of U and B parameters the former allows one to find the pair for which the structural similarity of the simulated and experimental image will be the highest. The latter, originally suggested for proton radiography data analysis in [9], relies on using a neural network trained on the simulation results in order to extract parameters of the fields in the interaction region.

6. Results for model targets

In this section proton radiography is discussed in application to several model targets. Their geometrical parameters are chosen in compliance with possible real targets which can be made by means of laser processing of metallic foils, etching, 3D printing and other methods.

One of possible geometries is hollow targets with curved internal surface – "snail-type" targets, which have already demonstrated their potential for strong quasi-stationary magnetic field generation [10,11]. The laser beam is sent into such target at a grazing incidence, which leads to the formation of a quasi-circular current circuit along the inner surface. Proton radiographs for two snail-type targets with different current directions probed perpendicularly to their axis are given in Figure 6.

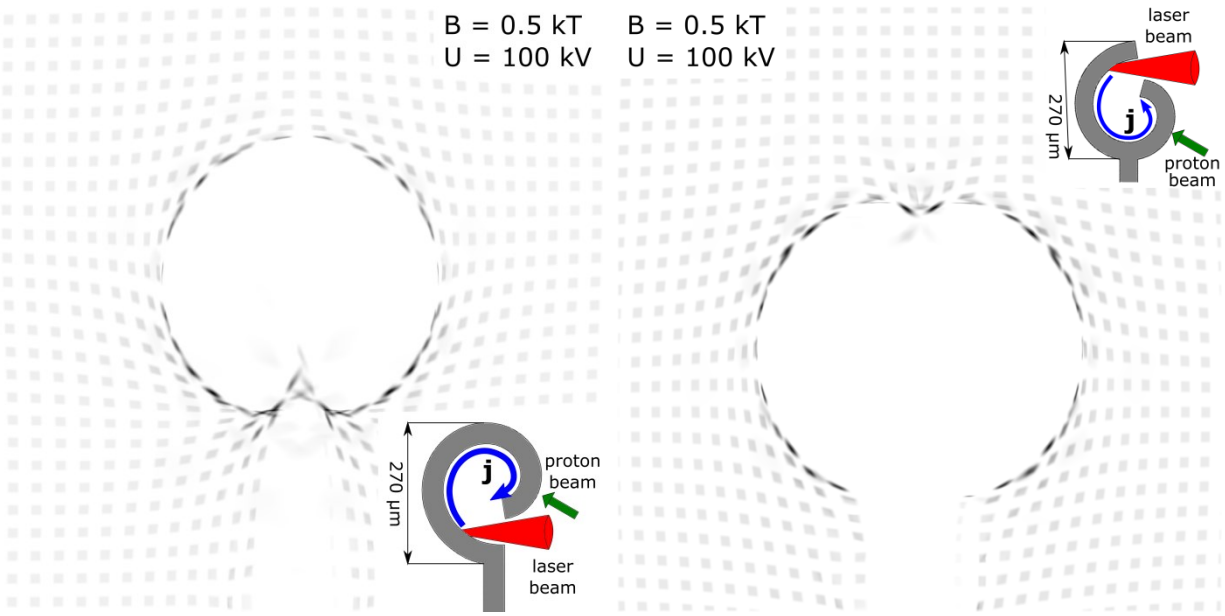

Figure 6. Proton radiographs for snail-type targets with different current flow directions probed perpendicularly to their axis; B and U are the magnetic field (at the geometric centre of the target) and the electric potential used in calculations.

Due to the fact that the shape of the current circuit for this target is close to a ring, the radiographs look similar to the one in Figure 3b, but with the clearly visible shadow of the target mounting post. The "caustics" part of the structure is reversed for two opposite current flow directions. Geometric parameters of this type of radiographs allow estimating electromagnetic fields using methods described in Section 5.

It is also possible to create discharge currents in snail targets in simpler irradiation geometry – by focusing a laser pulse on the inner tip of the snail. The generated currents in this case run along the target perimeter and partially along the target mounting post, creating strong magnetic field parallel to the target axis. Probing this target at an angle of 30° to its axis leads to a radiograph shown in Figure 7, left. The upper part of the radiograph resembles the structure on Figure 3d due to similarities in the shapes of current circuits of this target and a current ring target. In the left part of the region inside the "blob" one can observe a spot created by protons passing the central region of the snail and deflected by a vertical magnetic field component to the left. If magnetic fields in the central region of the snail reach the order of 1 kT, they may start to focus the proton beam coming at a small angle to the target axis, producing bright distorted spots inside the "blob" observed on the radiograph. This effect is demonstrated on the radiograph for axial probing geometry in Figure 7, right.

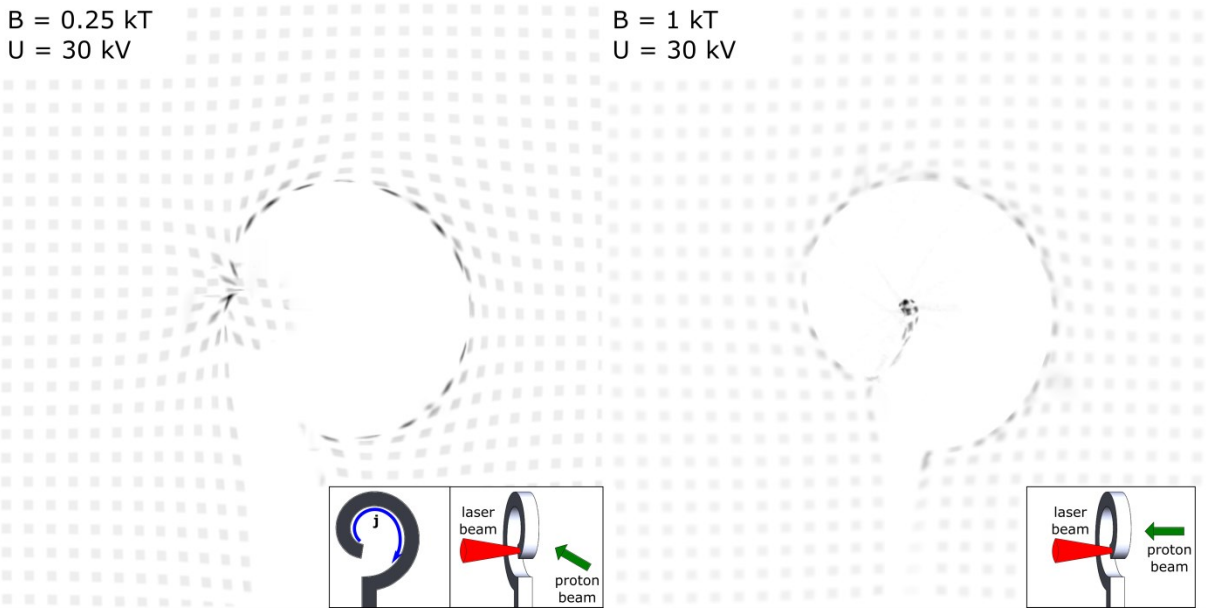

Figure 7. Proton radiographs for a snail-type magnetic field generator based on creating discharge currents by focusing a laser pulse on the inner tip of the snail. Left: proton probing is done at an angle of 30° to the target axis; right: probing is done parallel to the target axis.

Another interesting target geometry corresponds to chiral targets, originally suggested in [12]. The laser beam is directed into the central area of such a target where it undergoes multiple reflections from the tips of the "claws" of such a target and causes strong currents along the surface of these "claws". Simulated radiographs for chiral target probed at 0° and 15° to its axis are given in Figure 8.

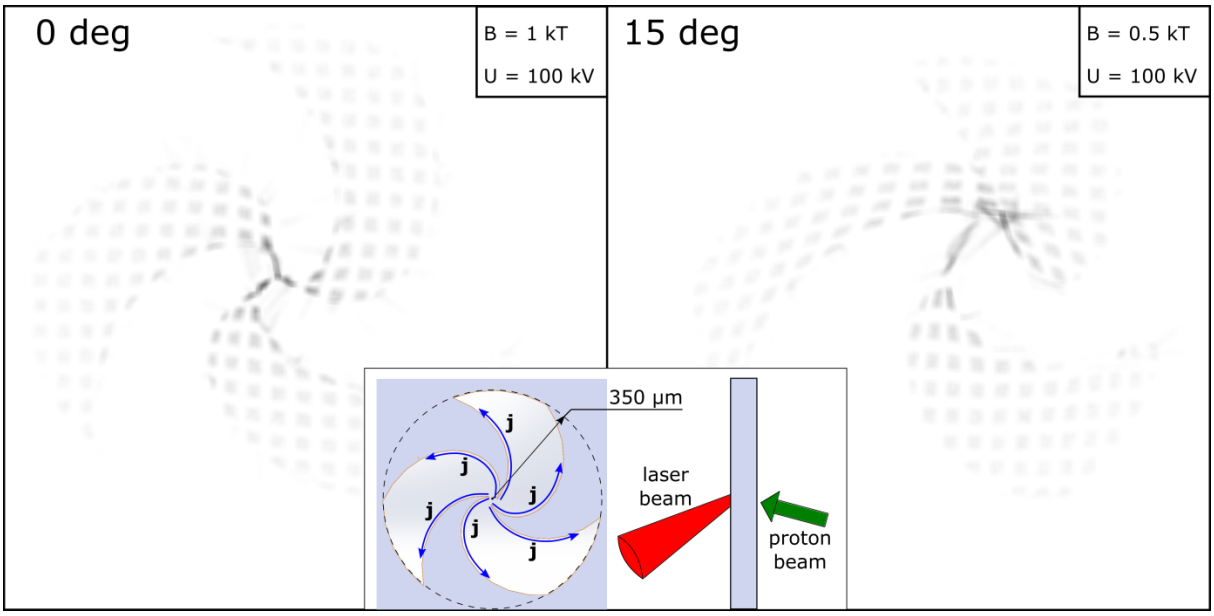

Figure 8. Proton radiographs for the chiral target probed along its axis (left) and at an angle of 15° to its axis (right); B and U are the magnetic field (at the geometric centre of the target) and the electric potential used in the calculations.

In the parallel probing geometry the radiograph can be describes as a "bloated" shadow of the target "claws" with some proton focusing observed in the centre of the image. The degree of focusing or collimation for protons travelling through the central region increases with the value of the

magnetic field which is showcased in Figure 9. For a non-parallel target probing geometry (15° to the target axis) the structure also resembles the "claws" shadow, but it is strongly distorted due to the magnetic field component deflecting protons sideways – in this case to the right and slightly up.

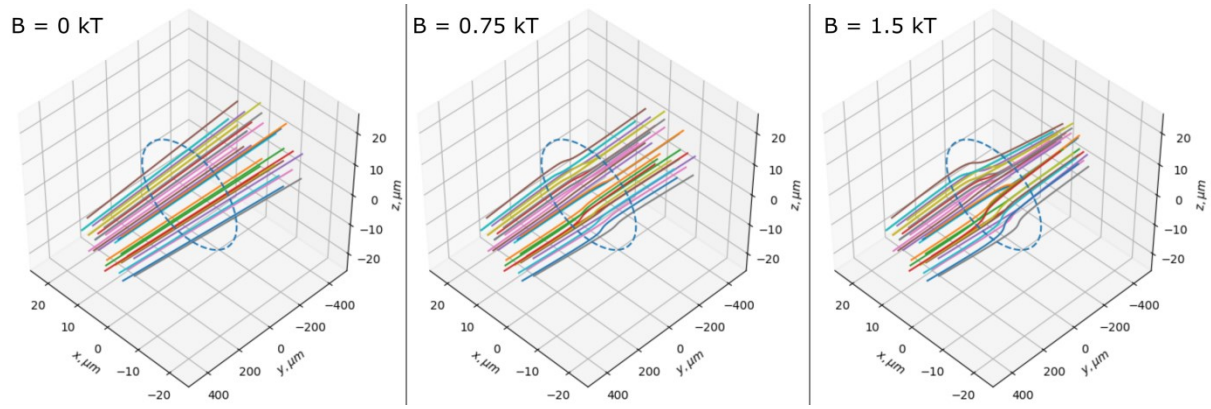

Figure 9. Illustration of proton beam collimation by magnetic fields of different strength generated at the centre of the chiral target; the dashed line represents the central area of the chiral target – from its geometric centre to the tips of the "claws". Note: the y-axis is not to scale with the x and z axes.

7. Conclusion

Despite its simplicity and possibility to perform data analysis for different target geometries, the approach described in this work has certain weak points. It relies on good understanding of the discharge current distribution in the target and surrounding plasma in order to calculate magnetic field for simulations and does not take into account fields created by expanding plasmas. This limitation may be overcome by using Particle-In-Cell simulations to characterize the current distribution in the interaction region and therefore the field structure. Another possible solution of this problem requires finding a general form of describing the magnetic field in the studied region. Using a neural network trained on a vast number of simulated radiographs for different values of parameters of this form may enable finding an optimal set of parameters for which maximum similarity with the experimental radiograph can be achieved.

Acknowledgement

The research leading to these results has received funding from LASERLAB-EUROPE (grant agreement no. 654148, European Union's Horizon 2020 research and innovation programme). The work was partially supported by the project # FSWU-2020-0035 (Ministry of Science and Higher Education of the Russian Federation).

References

[1] Fujioka S *et al.* 2013 Kilotesla magnetic field due to a capacitor-coil target driven by high power laser. *Sci. Rep.* **3** 1170
[2] Santos J J *et al.* 2015 *New J. Phys.* **17** 083051
[3] Ehret M *et al.* 2017 *News and Reports from HEDgeHOB* GSI-2017-2 19-20
[4] Roth M and Schollmeier M 2016 Ion acceleration – Target Normal Sheath Acceleration. *CERN Yellow Reports* **1** 231
[5] Nurnberg F *et al.* 2009 *Rev.Sci. Instrum.* **80** 033301
[6] Santos J J *et al.* 2018 *Phys. Plasmas* **25** 056705
[7] SRIM.EXE, (C) 1984-2013, James F. Ziegler
[8] Kugland N L, Ryutov D D, Plechaty C, Ross J S and Park H S 2012 *Rev. Sci. Instrum.* **83** 101301
[9] Chen N, Kasim M, Ceurvorst L, Ratan N, Sadler J, Levy M, Trines R, Bingham R and Norreys P 2016 Machine learning applied to proton radiography. *Phys. Rev. E* **95** 043305

[10] Ehret M *et al.* 2019 Kilotesla plasmoid formation by a trapped relativistic laser beam. arXiv:1908.11430 [physics.plasm-ph]
[11] Korneev Ph, d'Humières E and Tikhonchuk V 2017 *Phys. Rev. E* **91** 43107
[12] Korneev Ph, Tikhonchuk V and d'Humières E 2017 Magnetization of laser-produced plasma in in a chiral hollow target. *New J. Phys.* **19** 033023